

## Origin of the complex wetting behavior in Co-Pt alloys

Y. Le Bouar, A. Loiseau, and A. Finel

*Laboratoire d'Etude des Microstructures (LEM), ONERA-CNRS, BP72, 92322 Châtillon Cedex, France*

(Received 9 July 2003; published 18 December 2003)

In the Co-Pt system, a simple cooling experiment can drive a sample ordered in the tetragonal  $L1_0$  structure (CuAu type) close to the two-phase region involving  $L1_0$  and the cubic  $L1_2$  ( $\text{Cu}_3\text{Au}$  type) structure. Using transmission electron microscopy observations, we show that interfaces in the  $L1_0$  structure are decorated: orientational domain walls are wetted by a single layer of  $L1_2$  structure whereas three macroscopic layers ( $L1_2/L1_0/L1_2$ ) appear at the antiphase boundaries. We then analyze this complex behavior in the framework of the Ising model with interactions limited to first and second nearest neighbors. This approach is generic in the sense that it is the simplest one that reproduces the  $L1_0$  and  $L1_2$  ground states, without the specificities of the model with first nearest-neighbor interactions only. The finite-temperature properties of the various  $L1_0/L1_0$  interfaces are computed with a low-temperature expansion and cluster variation method calculations in the inhomogeneous tetrahedron-octahedron approximation. The results are in full agreement with our experimental observations concerning the wetting of interfaces.

DOI: 10.1103/PhysRevB.68.224203

PACS number(s): 61.30.Hn, 68.37.Lp, 68.35.Rh

### I. INTRODUCTION

Wetting of antiphase boundaries (APB's) by the disordered solid solution has been a focus of intensive research, both theoretically<sup>1-5</sup> and experimentally<sup>6-8</sup> (for general reviews see Refs. 9 and 10). Much less is known concerning wetting by an ordered phase, where new features are expected due to the degeneracy of the ordered structures. Indeed, in all generality, if wetting occurs, the system may display either one or several variants of the same ordered phase along the wetted interface.

Wetting of antiphase boundaries by an ordered phase has been recently studied in the Co-Pt system.<sup>11</sup> In the platinum-rich side of the phase diagram (see Fig. 1), Co-Pt alloys are chemically disordered on a fcc lattice at high temperature and ordered at low temperature according to either a cubic  $L1_2$  structure ( $\text{CoPt}_3$ ) or a tetragonal  $L1_0$  structure ( $\text{CoPt}$ ). Depending on the temperature and the alloy concentration there is a narrow concentration range where the two ordered phases coexist at equilibrium. Using this topology of the phase diagram, samples were first ordered in the cubic  $L1_2$  structure, then cooled and annealed close to the two-phase region involving  $L1_2$  and the tetragonal  $L1_0$  structure (arrow 1 in Fig. 1). Using transmission electron microscopy, it was shown that the APB's in the  $L1_2$  structure are decorated by the  $L1_0$  structure and that the  $L1_0$  variant formed during this wetting process is related to the characteristics of the APB's through a simple rule: the  $L1_0$  tetragonal axis is normal to the displacement vector of the APB's and the translational variant ensures the continuity of the platinum-rich cubic planes between the bulk and the wetting structure. This wetting phenomenon was analyzed theoretically using both a mean-field model and a Landau approach. Theoretical results showed that wetting of  $L1_2$  APB's by a  $L1_0$  layer does occur, with the same geometrical characteristics as the ones observed experimentally. Finally, the influence of the wetting phenomenon on the consequent microstructural evolution was studied in detail. Because the lattice parameters and the symmetries of the  $L1_0$  wetting layer differ from those of the

parent  $L1_2$  structure, coherency elastic strains are generated in the sample. The accommodation of the elastic strains transforms the initially isotropic wetting layer into either a plateletlike<sup>12</sup> or a sawtoothlike microstructure.<sup>13</sup>

The present work is also devoted to the wetting of interfaces by an ordered phase in the Co-Pt system. However, we focus here on the transformation path corresponding to a sample initially ordered in the  $L1_0$  structure. When the samples are cooled and annealed close to the  $L1_0+L1_2$  two-phase region (arrow 2 in Fig. 1), we expect the formation of  $L1_2$  layers along the interfaces in the  $L1_0$  phase. However, the situation is more complex in the present study than in Ref. 11, because ordering in the tetragonal  $L1_0$  structure leads to the formation of two kinds of interfaces: translational domain walls, also called APB's, and orientational domain walls (ODW's). In the first part of the paper, we use different electron microscope techniques to study the wetting of APB's and ODW's in the  $L1_0$  structure. We show that

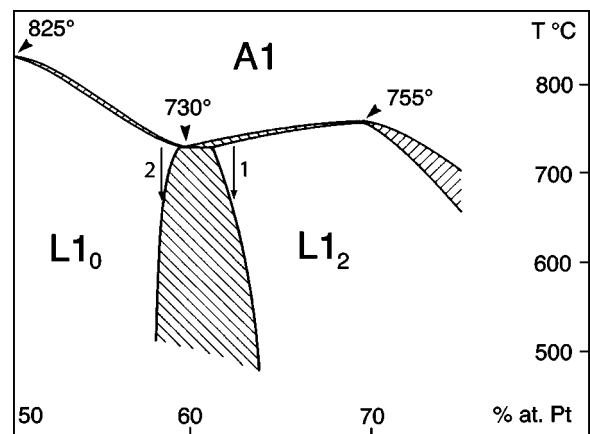


FIG. 1. Experimental Co-Pt phase diagram, determined by Leroux *et al.* (Ref. 14) and slightly modified using transmission electron microscopy (TEM) observations of a  $\text{Co}_{45}\text{Pt}_{55}$  sample (Ref. 22). Arrows 1 and 2 designate the annealing procedure used in Ref. 11 and in the present work, respectively.

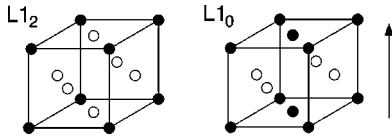


FIG. 2. Sketch of the  $L1_2$  and  $L1_0$  structures. The arrow designates the fourfold axis of the  $L1_0$  structure.

both kinds of interfaces are decorated but that the wetting phenomenon is qualitatively different. In particular, we will see that whereas the wetting of ODW's is rather simple, the wetting of APB's is not. As an example, surprisingly enough, the APB wetting layer consists of three consecutive sublayers of macroscopic thickness, instead of the usual single layer. In order to fully understand the experimental observations and to test the generic aspects of this complex behavior, we develop a theoretical approach based on a simple Ising model. We use the simplest Hamiltonian needed to stabilize  $L1_0$  and  $L1_2$  as ground states and we analyze the thermodynamical properties of the different interfaces along the  $L1_0/L1_2$  coexistence line, from 0 K up to the disordered phase. For this purpose, we develop simultaneously low-temperature expansions and inhomogeneous cluster variation method (CVM) calculations.

## II. EXPERIMENTAL PROCEDURE

### A. Sample preparation

The procedure followed for the sample preparation is the same as that used in previous works on Co-Pt alloys.<sup>14,15</sup> Alloys containing 59.5 or 60 at. % Pt were prepared by melting pure Co and pure Pt in an arc furnace in the form of small ingots which were homogenized during two days at 1000 °C under partial He pressure. Thin sheets (150  $\mu\text{m}$  thick) were obtained by rolling and disks were punched out of the sheets, sealed in evacuated quartz tubes under partial He atmosphere, annealed at 930 °C to remove strains induced by rolling, and water quenched. The disks were then annealed according to the following procedure: They were first heated up to 740 °C and then slowly cooled at a rate of 10 or 40 °C/24 h down to the temperature of interest, and finally maintained at this temperature during 2–4 weeks and quenched. As shown by Leroux *et al.*,<sup>14</sup> this procedure produces large ordered domains of the different phases at any temperature. Finally, the samples were thinned to electron transparency by Ar ion thinning and the surfaces were cleaned in aqua regia to remove the damaged areas produced by the ion bombardment. The microstructure studies were performed by TEM with a Jeol 4000FX working at 400 keV.

### B. Structures and imaging conditions

#### 1. Structures

The Co-Pt binary compounds are ordered at low temperature on the fcc lattice according to either the simple cubic  $L1_2$  structure (Cu<sub>3</sub>Au type) or the tetragonal  $L1_0$  structure (CuAu type). In the perfect  $L1_2$  structure (see Fig. 2), the Co atoms occupy the vertices of the cube and the Pt atoms its face centers. This structure displays four translational vari-

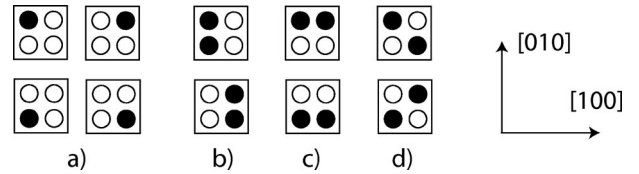


FIG. 3. Projection of the first nearest-neighbor tetrahedra (a)  $L1_2$  and (b)–(d)  $L1_0$  with a fourfold axis along  $[100]$ ,  $[010]$ , and  $[001]$ , respectively.

ants. The  $L1_0$  structure is formed by alternating (100) planes of cobalt and platinum. The structure is tetragonal and three orientational variants can be formed with two possible translational variants for each of them.

The fcc lattice can be decomposed into tetrahedra built on nearest neighbors. A conventional two-dimensional (2D) representation of this lattice is a projection along the  $[001]$  direction of two successive (001) atomic planes. The first nearest-neighbor tetrahedra are then represented by squares. All possible tetrahedra are listed in Fig. 3.

#### 2. Order parameter for the $L1_2$ and $L1_0$ structures

Since the  $L1_2$  and  $L1_0$  structures are, respectively, fourfold and sixfold degenerated, the description of the domain walls requires a multidimensional order parameter. A very convenient method consists in introducing the concentration wave formulation which takes advantage of the superstructure periodicity.<sup>16</sup> If  $c$  denotes the concentration of the minority species at site  $R$  of the binary alloy, one can write

$$c_R = c + \sum_{K \neq 0} c_K \exp(iK \cdot R), \quad (1)$$

where  $c$  is the mean concentration and  $K$  is a vector of the reciprocal lattice vector belonging to the first Brillouin zone of the fcc structure. To describe the  $L1_2$  and  $L1_0$  structures, only the  $K$  vectors of type  $[100]$  need to be considered, so that<sup>17</sup>

$$c_R = c + \eta_x \cos(k_x \cdot R) + \eta_y \cos(k_y \cdot R) + \eta_z \cos(k_z \cdot R), \quad (2)$$

where  $k_x = (2\pi/a)[100]$ ,  $k_y = (2\pi/a)[010]$ , and  $k_z = (2\pi/a)[001]$ . Here  $\eta = (\eta_x, \eta_y, \eta_z)$  is the three-dimensional order parameter. Because  $c_R$  has to be positive and smaller than 1,  $\eta$  should belong to the polyhedron defined by the following inequalities:

$$\begin{aligned} -c &\leq \eta_x + \eta_y + \eta_z \leq (1-c), \\ -c &\leq \eta_x - \eta_y - \eta_z \leq (1-c), \\ -c &\leq -\eta_x + \eta_y - \eta_z \leq (1-c), \\ -c &\leq -\eta_x - \eta_y + \eta_z \leq (1-c). \end{aligned} \quad (3)$$

In this formalism, the origin ( $\eta=0$ ) represents the disordered phase, where all sites are occupied with the same probability. The six possible  $L1_0$  variants correspond to the six cubic semiaxes:  $\eta = \pm \eta[100]$ ,  $\pm \eta[010]$ ,  $\pm \eta[001]$ . Simi-

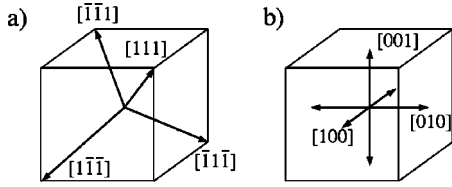


FIG. 4. Three-dimensional representation of the long-range-order (LRO) parameter for the  $L1_2$  (a) and  $L1_0$  (b) structures.

larly, the four translational variants of the  $L1_2$  structure (with the same stoichiometry  $A_3B$ ) are represented by  $\eta = \eta[111]$ ,  $\eta[1\bar{1}\bar{1}]$ ,  $\eta[\bar{1}\bar{1}1]$ , and  $\eta[\bar{1}\bar{1}\bar{1}]$  in  $\eta$  space.<sup>4,18</sup> A representation of the  $L1_0$  and  $L1_2$  variants in the (long-range-order) parameter space is shown in Fig. 4.

One can therefore describe the variants of  $L1_0$  and  $L1_2$  structures within the same formalism using the three-dimensional order parameter  $\eta$ . As we will see, this formalism is very useful to explain the wetting process observed in our Co-Pt samples.

### 3. Imaging conditions

The  $L1_2$  and  $L1_0$  structures can be distinguished in transmission electron microscopy by using the dark-field technique in two-beam conditions involving superstructure reflections. The method is here shortly recalled. More details can be found in Refs. 14 and 15. For all the observations, the foil was oriented with a  $[001]$  cube axis nearly parallel to the incident beam. This orientation is very convenient since the corresponding zone axis displays the different kinds of superstructure reflections produced by both  $L1_2$  and  $L1_0$  structures: namely,  $(100)$ ,  $(010)$ , and  $(110)$ . Three different dark-field (DF) images were obtained with the  $(120)$ ,  $(210)$ , and  $(110)$  reflections. Here  $(120)$  and  $(210)$  reflections were used instead of  $(100)$  and  $(010)$  since they are more easily attained in two-beam conditions.<sup>8,14</sup>

In the kinematic approximation, the DF intensity corresponding to a given structure is proportional to the square of the structure factor. Except for a weak variation of the form factor between the  $(120)$ ,  $(210)$  beams and the  $(110)$  beam, these three beams have similar structure factors in the  $L1_2$  phase. On the other hand, for a given orientation variant of the  $L1_0$  structure, the specific form of the structure factor gives rise to extinctions for two beams and the structure factor of the third one is larger than those of  $L1_2$ . As a consequence, for a given  $(120)$ ,  $(210)$ , or  $(110)$  DF, a  $L1_0$  zone appears either black or brighter than the  $L1_2$  zones, depending on the orientation of the tetragonal axis. As shown in Table I, this contrast rule allows us to distinguish between the different  $L1_0$  orientational variants and the  $L1_2$  phase. For convenience, we have introduced in Table I three levels of illumination: black (extinction), gray ( $L1_2$ ), and white ( $L1_0$ ). This contrast rule has been successfully used to characterize the microstructures of the two-phase  $L1_2+L1_0$  Co-Pt alloys.<sup>14,15</sup>

High-resolution electron microscopy (HREM) images of the structures projected along the  $[001]$  cubic axis have been used in addition to the dark-field images. Since the lattice

TABLE I. Contrasts in dark-field images using superstructure reflections in a  $[001]$  zone axis.

$\eta$	$L1_0$ structure			$L1_2$ any
	$\pm 100$	$\pm 010$	$\pm 001$	
$(120)$ DF	white	black	black	gray
$(210)$ DF	black	white	black	gray
$(110)$ DF	black	black	white	gray

parameter of both  $L1_0$  and  $L1_2$  is about  $3.8 \text{ \AA}$ , we were limited to superstructure images obtained by selecting the  $\{100\}$  and  $\{110\}$  superstructure reflections with an objective aperture of  $9 \text{ nm}^{-1}$ . The EMS code<sup>19</sup> has been used to simulate the patterns corresponding to our imaging conditions. As shown in Ref. 11, for wide ranges of thickness ( $4\text{--}20 \text{ nm}$ ) and (negative) defocus ( $60\text{--}120 \text{ nm}$ ), the HREM image of the  $L1_2$  structure consists of a pattern formed by intense bright dots located on the Co-rich columns. HREM images of a  $L1_0$  structure with a fourfold axis normal to the incident beam show regularly spaced fringes normal to the fourfold axis and located above the Co-rich planes for the same range of thickness and defocus. This type of HREM images provides therefore a direct analysis of both the structure and the type of variant.

## III. EXPERIMENTAL RESULTS

The phase diagram determined by Leroux *et al.*<sup>14</sup> and shown in Fig. 1 was used to choose the alloy concentrations and annealing temperatures. Numerous samples with an atomic concentration of platinum of 59.5% or 60% were prepared and first ordered in the  $L1_0$  state. The annealing temperature was then progressively reduced down to a temperature close to the limit of the  $L1_2+L1_0$  stability region. Therefore, the final temperatures described in Sec. II A were chosen between  $600$  and  $690 \text{ }^\circ\text{C}$ .

Images of a typical microstructure are shown in Fig. 5. The microstructure consists of alternating  $L1_0$  platelets of two orientational variants. The platelets are parallel to  $\{110\}$  planes. Such a geometry is widely observed after coherent ordering of a tetragonal structure because the associated volume-dependent part of the elastic energy is zero.<sup>16,20,21</sup> However, as clearly shown by the white contrast in Fig. 5(a), the interfaces between the  $L1_0$  domains are decorated.

### A. Wetting of ODW's

Consider first the orientational domain wall (ODW). By comparing the three dark fields  $(110)$ ,  $(210)$ , and  $(120)$  in a  $[001]$  zone axis, we see that the ODW are decorated by a small layer with a contrast obeying exactly the rules for  $L1_2$  ordering. Between two platelets, the width of the layer is about  $3 \text{ nm}$ . Near the ends of the platelets, the  $L1_2$  layer becomes thicker and transforms into a triangular-shaped domain (see  $a, b, c$  in Fig. 5). This specific shape is due to the relaxation of the elastic strain energy as shown elsewhere.<sup>22</sup> To fully characterize the  $L1_2$  layer, we have also to determine which one among the four possible translational vari-



FIG. 5. Dark-field images of wetted interfaces in the  $\text{Co}_{40}\text{Pt}_{60}$  alloy aged at 690 °C: (110), (b) (210), and (c) (120).

ants is formed. A very convenient way to get such an information is to make HREM images of the decorated ODW with the foil normal oriented along the [001] direction. An example of a HREM image is presented in Fig. 6. Following Ref. 11, we have compared our images with simulation patterns obtained with the EMS code. The result of our analysis is that the translational variant of the  $L1_2$  structure formed during the wetting process is such that its platinum-rich cubic planes are also platinum-rich planes in the two  $L1_0$  domains. The atomic structure of a wetted ODW is sketched in Fig. 6(b), where the platinum-rich cubic planes are pointed out by dashed lines.

The observed selection rule of the  $L1_2$  translational variant can also be conveniently visualized using the 3D order parameter presented above. As can be seen in Fig. 7(a), among the four possible  $L1_2$  variants (dashed arrows), the observed LRO parameter of the layer is always characterized by a positive scalar product with the LRO parameters of the neighboring  $L1_0$  domains. It can also be pointed out that the LRO parameter of the  $L1_2$  layer always provides the shortest path in the 3D LRO parameter space between the LRO parameters of the  $L1_0$  bulk domains (solid arrow). This point can be rationalized by studying the shape of the free energy

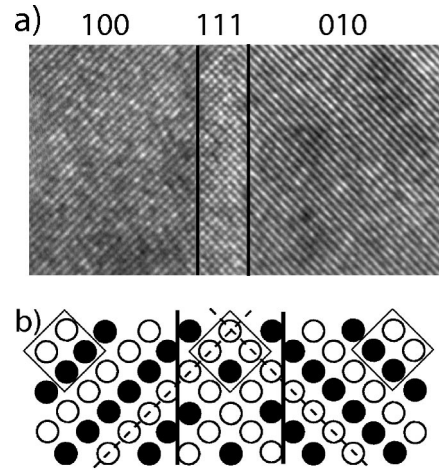


FIG. 6. (a) HRTEM image of a wetted ODW in the  $\text{Co}_{40}\text{Pt}_{60}$  sample aged at 600 °C. The LRO parameters corresponding to the bulk  $L1_0$  domains and to the  $L1_2$  layers are indicated above. In the  $L1_2$  region bright dots are located on the Co-rich columns and in the  $L1_0$  regions white fringes are located on the Co-rich planes. (b) Sketch of the corresponding atomic configuration. The dashed lines indicate the platinum-rich cubic planes common to the  $L1_2$  and  $L1_0$  structures.

hypersurface as a function of the components of the LRO parameter (for example, see Refs. 11 and 23), but this study is beyond the scope of the present paper.

**B. Wetting of APB's**

We have found that the APB's in the  $L1_0$  structures are also wetted. However, the wetting process of the antiphase boundaries is qualitatively different from that of the ODW. Indeed, as can be seen in Fig. 5 and in the close-up in Fig. 8, three new layers have appeared: two new  $L1_2$  layers with a new  $L1_0$  layer in between. These layers are only a few nanometers thick. The dark-field technique allows us to show that the fourfold axis of the new  $L1_0$  layer is always normal to that of the  $L1_0$  domains forming the APB. More precisely, as can be seen in Fig. 8, the fourfold axis of the new  $L1_0$  layer is that of the neighboring  $L1_0$  platelet. The formation of three new layers is a rather surprising phenomenon. It implies that the sum of the four  $L1_0/L1_2$  interfacial energies is lower than the interfacial energy of the initial APB.

It is most interesting to point out that the formation of the three layers ( $L1_2/L1_0/L1_2$ ) transforms the initial APB into two successive ODW's which are both wetted by the  $L1_2$

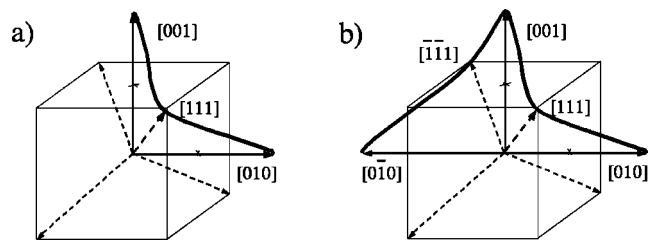


FIG. 7. Sketch of the 3D profile of the LRO parameters across a wetted ODW (a) and a wetted APB (b).

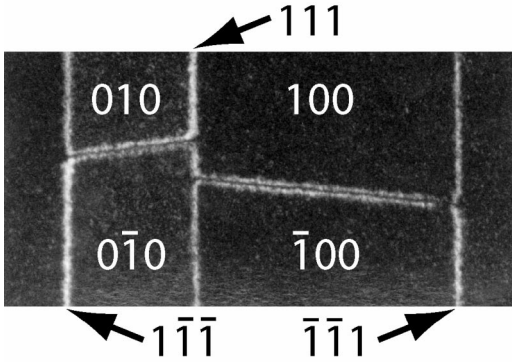


FIG. 8. 110 dark-field image of wetted interfaces in the  $\text{Co}_{40}\text{Pt}_{60}$  alloy aged at 690 °C. The LRO parameters corresponding to the bulk  $L1_0$  domains and to the  $L1_2$  layers are indicated.

structure. Therefore the criterion presented above for the selection of the  $L1_2$  translational variant during the wetting of an ODW can be applied here to deduce the selection of the translational variants of the  $L1_2$  layers formed during the wetting of APB's. The profile of the LRO parameters across a wetted ODW is sketched in Fig. 7(b).

Finally, wetted APB's have different orientations. Some of them are imaged with a sharp contrast as those shown in Fig. 8. They are edge on, flat, and present a deviation of approximately 5.5° with the  $\langle 110 \rangle$  directions. More precisely, even if APB's are globally flat, they may contain ledges at the atomic scale. This point could be clarified with HREM observations and simulations. However, the CVM calculations presented below show that the peculiar wetting phenomenon observed here is not linked to the existence of atomic ledges. In brief, we did not undertake any precise analysis of the possible ledges because, as explained below, they do not play any pertinent role in the wetting phenomenon studied here. Note also that in Fig. 5 we observe diffuse contrasts which are related to APB's which are inclined with respect to the electron beam.

#### IV. THEORETICAL MODELING

In this section, we present the theoretical framework that we have used to study the wetting behavior of interfaces observed in the Co-Pt system. We first detail the energetical model and its bulk ground-state configurations. Then we present the cluster variation method and the low-temperature expansion that are used in the following sections to characterize the wetting at finite temperature.

##### A. Ising model at 0 K with interactions up to second nearest neighbors

The Ising model applies quite naturally to binary alloys where the two-valued spin variable denotes the nature of the atom at each site. The choice of such a Hamiltonian can be justified from the electronic structure of the alloy by using the so-called generalized perturbation method.<sup>18,24</sup> Our approach is limited to a perfect fcc lattice with interactions up to second nearest neighbors. The grand-canonical energy  $E$  can then be written as

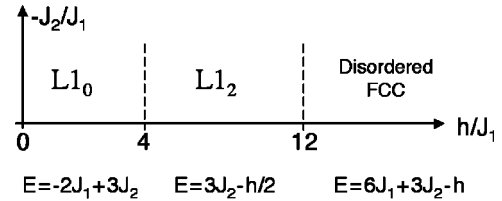


FIG. 9. Ground states and associated energies per site for the fcc lattice ( $J_1 > 0$ ,  $J_2 < 0$ ).

$$E = \frac{1}{2} J_1 \sum_{n,m} \sigma_n \sigma_m + \frac{1}{2} J_2 \sum_{n,m} \sigma_n \sigma_m - h \sum_n \sigma_n, \quad (4)$$

where  $\sigma_n = 1$  when site  $n$  is occupied by an atom of cobalt and  $\sigma_n = -1$  otherwise. The first and second sums run over the first and second nearest neighbors, respectively, and  $h$  plays the part of a chemical potential difference.

Within our simple approach limited to second nearest neighbors, the occurrence of a phase diagram involving the  $L1_0$  and  $L1_2$  phases (as observed in the Co-Pt system) requires a positive  $J_1$  and a negative  $J_2$ . The homogeneous ground states of this model are well known (see, for example, Ref. 18). The results are recalled in Fig. 9. Because we are only interested in the  $L1_2 + L1_0$  stability region, the chemical potential  $h$  should be equal to  $h_c = 4J_1$ .

In fact, the  $J_1 - J_2$  model is the simplest approach adapted to our experimental situation. If we do not take into account  $J_2$ ,  $L1_0$  and  $L1_2$  would still be ground states, but the  $L1_0/L1_2$  equilibrium point at 0 K would be infinitely degenerated, with a finite residual entropy (see, for example, Ref. 25). As a consequence, the thermodynamics of the  $L1_0/L1_2$  interfaces would be very specific to the model.

##### B. Cluster variation method and the tetrahedron-octahedron approximation

We need now to investigate the finite-temperature behavior of the different interfaces that we observed or that we may anticipate. Quite naturally, we expect that the free energy differences between the different configurations are very small. Indeed, as shown below (see, e.g., Table III), the free energy difference between the competitive interface configurations may be as small as  $10^{-5} J_1$  per site of the interface. Therefore we need a very accurate approach which should, moreover, handle inhomogeneous situations. The simplest solution would probably consist in using the Monte Carlo method. However, this approach is very time consuming for large systems and, more importantly, does not provide a straightforward way to compute free energies with the precision needed here to predict the more stable interface configurations. Therefore, we used the CVM which has already been used to study wetting and pinning phenomena in fcc systems.<sup>2,26</sup> The CVM is a variational theory in which the correlations which extend beyond the size of selected maximum clusters are neglected (see, for example, Refs. 18,27,28). In other words, the total entropy is written as a linear combination of the entropies of the finite clusters:

$$S^{CVM} = \sum_{\alpha}' a_{\alpha} S_{\alpha}, \quad (5)$$

$$S_{\alpha} = -k_B \sum_{C_{\alpha}} \rho_{\alpha}(C_{\alpha}) \ln[\rho_{\alpha}(C_{\alpha})],$$

where  $S_{\alpha}$  is the entropy of cluster  $\alpha$  and  $\rho_{\alpha}(C_{\alpha})$  the probability of cluster  $\alpha$  being in configuration  $C_{\alpha}$ . The prime in the first sum means that we consider only the clusters that are included in at least one maximum cluster and the coefficients  $a_{\alpha}$  are geometric constants that take into account the overlapping of the clusters. An important point is that the probabilities  $\rho_{\alpha}(C_{\alpha})$  are not independent. For the purpose of the minimization procedure it is best to expand the cluster probabilities in terms of linear combinations of independent variables, the so-called correlation functions:

$$\rho_{\alpha}(\{\sigma_n, n \in \alpha\}) = \frac{1}{2^{|\alpha|}} \left[ 1 + \sum_{\beta \subset \alpha} \left( \prod_{n \in \beta} \sigma_n \right) \left\langle \prod_{n \in \beta} \sigma_n \right\rangle \right], \quad (6)$$

where the index  $n$  is used to label the sites,  $|\alpha|$  is the number of sites in cluster  $\alpha$ ,  $\langle X \rangle$  represents the ensemble average of  $X$ , and  $\langle \prod_{n \in \beta} \sigma_n \rangle = \langle \sigma_{\beta} \rangle$  is the correlation function of cluster  $\beta$ . The CVM free energy is then given by

$$F^{CVM}(\{\sigma_{\beta}\}) = \frac{1}{2} J_1 \sum_{n,m} \langle \sigma_n \sigma_m \rangle + \frac{1}{2} J_2 \sum_{n,m} \langle \sigma_n \sigma_m \rangle - h \sum_n \langle \sigma_n \rangle - T S^{CVM}(\{\sigma_{\beta}\}), \quad (7)$$

where the internal energy defined by  $U = \langle E \rangle$  has been expressed in the specific case of Eq. (4). The free energy is thus a functional of all the correlation functions  $\langle \sigma_{\beta} \rangle$  of the clusters  $\beta$  that are included in at least one of the preselected maximum clusters. Of course, the first and second nearest-neighbor correlation functions are among them, as the maximum clusters should obviously contain the interactions that we want to consider.

The equilibrium state is obtained by the minimization of Eq. (7). Considering only first and second neighbor interactions, it is well known that the minimum CVM approximation that can be used is the tetrahedron-octahedron one (CVM-TO).<sup>29–31</sup>

To investigate the thermodynamic properties of the interfaces, we must first determine the equilibrium phase diagram for the homogeneous phases. Using the CVM-TO, the phase diagram that we have obtained when  $J_2/J_1 = -0.2$  is presented in Fig. 10. For temperatures above  $T = 2.88J_1/k_B$ , the only stable structures are  $L1_0$ ,  $L1_2$ , and the disordered fcc. Because we are only interested here in inhomogeneous CVM calculations at temperature above  $T = 2.88J_1/k_B$ , we did not need to determine the stability region of the  $L'$  structure which may appear at lower temperature (see, for example, Refs. 18 and 25). Note that when the temperature increases, the domain of stability of the  $L1_2$  phase grows at the expense

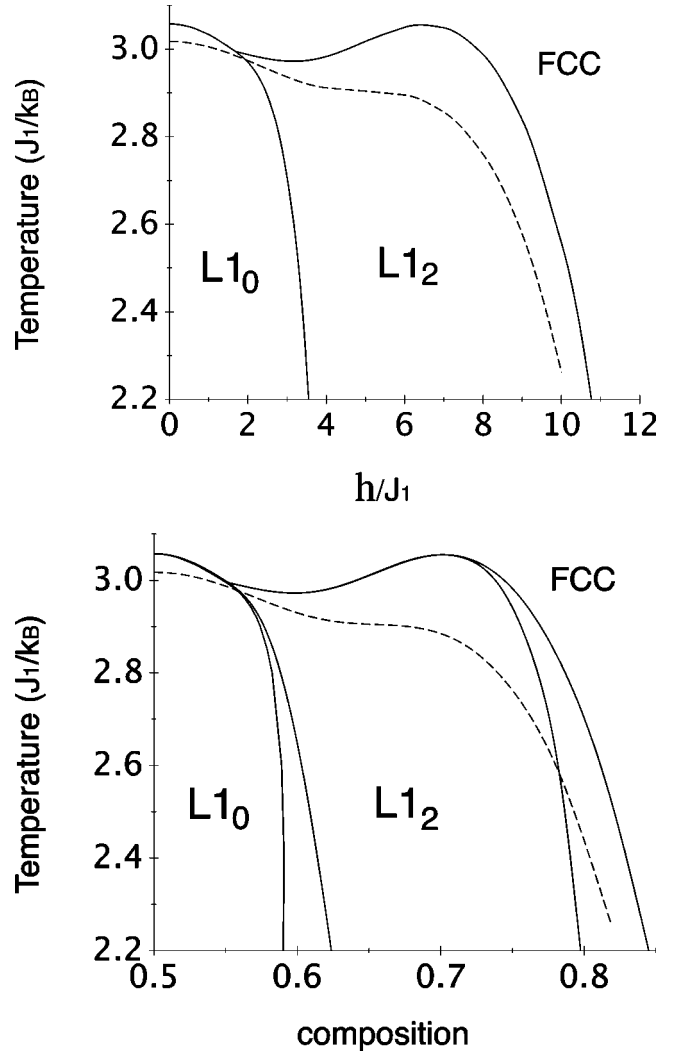


FIG. 10. Grand-canonical and canonical CVM-TO phase diagrams with  $J_2/J_1 = -0.2$ . The dashed line is the  $\langle 100 \rangle$  ordering spinodal. The triple point, where the disordered  $L1_0$  and  $L1_2$  phases meet, is given by  $kT = 2.994620J_1$  and  $h = 1.681507J_1$ .

of that of the  $L1_0$  phase. This point is confirmed by a low-temperature expansion of the  $L1_0$  and  $L1_2$  free energies (see below).

Our aim is to analyze the finite-temperature behavior of the interfaces. Therefore, we need to consider inhomogeneous situations. This increases dramatically the number of variational parameters. In order to keep the computation tractable, we will consider that the system is translationally invariant along the directions parallel to the interface plane and inhomogeneous along the remaining perpendicular direction. This means that we do not take into account the fluctuations along the interface. In other words, we suppose that the temperature is below any roughening transition temperature and that the interface is flat. As shown in Fig. 5, this point is consistent with the experimental behavior in the Co-Pt samples. In any case, if a roughening process were taking place, it would not be possible to reproduce it with the approach used here. Indeed, as explained above, the CVM is a variational approach which consists in neglecting the corre-

lation that extend beyond a given finite range. Therefore, the long-range fluctuations responsible for the roughening transition are not taken into account. As a result, even if the interface was embedded into a three-dimensional simulation box, the variational procedure would lead to a flat interface.<sup>44</sup>

The inhomogeneous system we have used is of the form  $1 \times 1 \times n$  in units of fcc cubes, along the cubic directions, with  $n$  ranging from 100 to 300. Large  $n$  values are needed because we intend to reproduce multiwall equilibrium states that incorporate wetting phenomena. As a result, even though we have reduced the dimensionality of the calculation box, the number of variational parameters is still important as there are 120 correlation functions per fcc cube. In order to handle any kind of interface configuration, we used two independent mirror boundary conditions along the direction perpendicular to the interface.

We now comment on the minimization procedure that we have used. Even though the number of independent variational parameters is huge (a few  $10^4$ ), we used a second-order algorithm, which needs the computation of the Hessian of the free energy—i.e., the matrix of the second derivatives of  $F^{CVM}\{\{\sigma_\beta\}\}$ . Taking advantage of the band structure of the Hessian and, most importantly, of the fact that we have an explicit analytical formula for the second derivatives, we found that this algorithm does not require a large memory or a huge CPU time.

A second-order algorithm is in fact required to reach the precision needed here. As we will see below (for example, in Table III) a typical interface free energy is of the order of a few  $10^{-2}J_1$  and can be as small as a few  $10^{-4}J_1$  (per site of the interface plane). We want to compare different interface configurations. As each interface energy is calculated through the difference between two configurations whose total free energies are of the order of a few  $10^3J_1$ , the relative precision needed for each total free energy minimization is of the order of  $10^{-8}$ . This precision can only be reached with a minimization scheme that ensures a quadratic convergence and, due to the huge number of variational parameters that we must handle here, whose number of iterations does not depend explicitly on the dimension of the parameter space. These two conditions are fulfilled with the second-order algorithm used here.

For all the CVM calculations presented below, the initial configuration for the minimization procedure is always a perfectly abrupt interface between two bulk phases previously equilibrated at the values of the temperature and of the chemical potential that we want to consider. Of course, we must wonder whether the equilibrium state that is reached is a global minimum. This will not be guaranteed, in particular, if layering effects due to the discrete character of the lattice are present. However, as we will see below, any individual interface that appears in the various APB's or ODW's analyzed here is relatively large: a typical thickness is of the order of ten fcc cubes. This is due to the fact that we consider relatively high temperatures, which are close to the spinodal temperature of the  $\langle 100 \rangle$  concentration wave. As a result, the correlation lengths are large. This leads to broad interfaces

and, consequently, to a weak pinning on the lattice and, indeed, we did not observe any layering effects.

### C. Low-temperature expansion

As we will see below, the stability analysis of interfaces at 0 K sometimes leads to several configurations associated with the same energy. The CVM in its inhomogeneous implementation will be able to lift the degeneracy and the results will be in agreement with experimental observations. However, the CVM analysis consists in a closed-form minimization scheme which does not provide with a simple way to understand the origin of the stabilization of a particular interface configuration. Thus we have found most useful to complete our CVM analysis with a low-temperature expansion of the free energy,<sup>32,33</sup> in which the local mechanism responsible for the finite-temperature stabilization is clearly identified.

Low-temperature expansions have already been proposed to analyze the thermodynamical properties of interfaces in the fcc lattice.<sup>34,35</sup> However, the method used in these analyses differs from the one proposed here, in that we control the expansions by ordering the excitation energies in ascending order instead of using the number of spin flips involved in the excitations.

We now briefly sketch the underlying formalism. Suppose that the ground state for a particular value  $h_c$  of the chemical potential is degenerated between two configurations, labeled 1 and 2. The ground-states energies are thus equal for  $h = h_c$ :

$$\mathcal{E}_1(h_c) = \mathcal{E}_2(h_c). \quad (8)$$

At finite but low enough temperature, we expect that the equilibrium state corresponds to a small perturbation of one of the ground states. This point, which has been rigorously proved when the number of degenerated ground states is finite, requires the two following properties: any two ground states must differ by an infinite number of lattice site configurations and the excess energy  $\Delta E(C_h^i)$  of a finite perturbation (defined below) of one of the ground state configurations must increase with the size of the perturbation. A finite perturbation  $C_h^i$  of the ground state  $i$  is defined as the process of flipping simultaneously the occupancy of all the sites within a finite cluster  $C_h$  embedded into the ground state  $i$ . These two conditions ensure that, at low enough temperature and in the limit of an infinite system, the low-temperature expansions that we define below converge and that the true free energy corresponds to the smallest of the expansions. We may then proceed as follows. We first introduce the free energy expansion linked to a given ground state  $i$  by

$$\mathcal{F}_i(h, T) = \mathcal{E}_i(h) - kT \sum_{C_k^i} \exp[-\beta \Delta E(C_k^i)], \quad (9)$$

where the sum runs over the excitations  $C_k^i$  of the ground state  $i$ . Now we collect together all the perturbations which have the same excitation energy and write Eq. (9) as

TABLE II. Contribution to the ground-state energy per site  $E_{g.s.}$ , energy increase  $\Delta E$  when flipping the site occupancy, and degeneracy  $\mu$  of each type of site in the  $L1_0$  and  $L1_2$  structures.

	$E_{g.s.}$	$\Delta E$	$\mu$
$\circ_{L1_0}$	$-h - 2J_1 + 3J_2$	$16J_1 - 12J_2$	1/2
$\bullet_{L1_0}$	$+h - 2J_1 + 3J_2$	$-12J_2$	1/2
$\circ_{L1_2}$	$-h + 2J_1 + 3J_2$	$-12J_2$	3/4
$\bullet_{L1_2}$	$+h - 6J_1 + 3J_2$	$16J_1 - 12J_2$	1/4

$$F_i(h, T) = E_i(h) - kT \sum_n \mu_n^i \exp(-\beta \Delta E_n), \quad (10)$$

where the index  $n$  labels the different excitation energies and  $\mu_n^i$  is the degeneracy (per site) of excitation  $n$  in the ground state  $i$  and where  $F_i(h, T)$  and  $E_i(h)$  are the free and ground-state energies (per site) of ground state  $i$ . The calculation of the coefficients  $\mu_n^i$  is not always simple, as it may involve connected as well as nonconnected clusters (two atoms are connected if they are linked by an interaction). However, an important exact simplification arises when we are interested only in free energy differences between two ground states—say, states 1 and 2: the degeneracies  $\mu_n^i$  of the first excitation energy  $\Delta E_n$  that differentiates between two states (i.e., the smallest one for which  $\mu_n^1 \neq \mu_n^2$ ) differ only by the number of connected clusters. This simplifies greatly the identification of the equilibrium state at finite temperature.

In the present situation, we want to analyze the stability of different interface configurations in the wetting regime—i.e., when we approach the  $L1_0/L1_2$  equilibrium line at finite temperature. Therefore, we first need to locate this line in the  $(h, T)$  plane. This amounts to performing a low-temperature expansion of the two bulk phases  $L1_0$  and  $L1_2$  in the neighborhood of the point  $(h_c = 4J_1, T = 0)$ . As a result, Eq. (10) tells us that, if  $\Delta E_{n_0}$  is the first excitation with  $\mu_{n_0}^{L1_0} \neq \mu_{n_0}^{L1_2}$ , the equilibrium line  $h(T)$  is, to the lowest order in  $kT$ , the solution of

$$E_{L1_0}(h) - E_{L1_2}(h) = kT(\mu_{n_0}^{L1_0} - \mu_{n_0}^{L1_2}) \exp\left(-\frac{\Delta E_{n_0}}{kT}\right). \quad (11)$$

It happens here that, when  $J_2 < 0$ , the first excitation energy whose degeneracies differ in  $L1_0$  and  $L1_2$  structures corresponds to a single spin flip. In Table II, we display all the single-spin-flip energies in  $L1_0$  and  $L1_2$  structures, together with their degeneracies: at the  $L1_0/L1_2$  equilibrium point ( $h_c = 4J_1$ ), the lowest excitation energy is  $\Delta E_{n_0} = -12J_2$ . In fact, as long as we are only interested by the  $L1_0/L1_2$  equilibrium line, we just need to estimate the excess energies for  $h = h_c$ . Indeed, we may anticipate that, at finite but low temperature, the shift  $\Delta h(T) = h(T) - h_c$  of the equilibrium chemical potential from its  $T = 0$  K value will decrease exponentially with  $-\Delta E_{n_0}/(kT)$  because the left-hand side (LHS) of Eq. (11) is linear in  $\Delta h$ . As a result, we can neglect the  $T$  dependence of  $h(T)$  in the RHS of Eq. (11) and replace

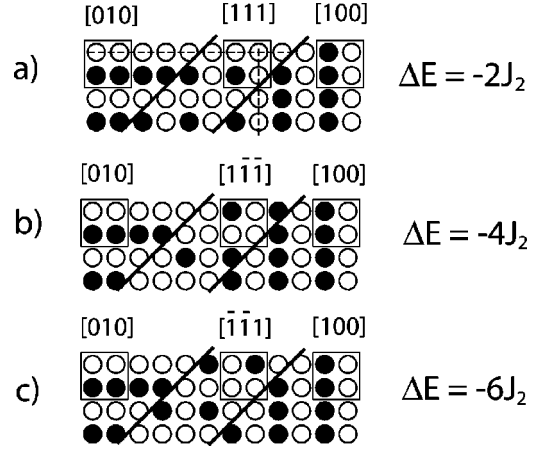


FIG. 11. Excess energy cost at 0 K of different ODW's wetted by the  $L1_2$  structure. The 3D LRO parameter is indicated on the top of each domain. The dashed lines in (a) point out the continuity of the majority atom planes between the structures.

$h$  by  $h_c$ . In the present situation, the ground-state energies of the  $L1_0$  and  $L1_2$  phases may be computed with the informations given in Table II, and we get

$$\Delta h(T) = h(T) - h_c = -\frac{kT}{2} \exp\left(\frac{12J_2}{kT}\right). \quad (12)$$

The  $L1_0/L1_2$  equilibrium line is thus bended towards the low  $h$  values. In other words, at  $h = h_c$  and finite temperature,  $L1_2$  is more stable than  $L1_0$  because it contains more low-energy excitations than  $L1_0$ . This is in agreement with the low-temperature shape of the phase diagram calculated within the CVM-TO (see Fig. 10).

Finally, we note that the precision of the expression for the equilibrium line given in Eq. (12) is governed by the next lowest excitation energy whose degeneracies in  $L1_0$  and  $L1_2$  differ. It is easy to convince oneself that this excitation energy is  $\Delta E_{n_1} = -20J_2$ . Therefore, the relative precision of  $\Delta h(T)$  in Eq. (12) is of the order of  $\exp(8J_2/kT)$ . We conclude that Eq. (12) is valid provided  $kT/J_1 \ll 8|J_2|/J_1 \sim 1.6$  (with the ratio  $J_2/J_1 = -0.2$  used here).

## V. WETTING OF ODW'S IN THE $L1_0$ STRUCTURE

In the following sections, we detail the predictions of our theoretical approach for the wetting of interfaces in the  $L1_0$  phase. The present section is devoted to the ODW's. The multiple-layer wetting behavior of APB's will be studied in the next two sections.

### A. $T = 0$ K

Let us first consider an ODW between two  $L1_0$  variants wetted by the  $L1_2$  structure. As observed experimentally (see Fig. 5), we consider a flat ODW oriented in a  $\{110\}$  plane. The question is to know which  $L1_2$  variant provides the minimum energy for a given ODW.

As shown in Fig. 11, we have introduced a slice of  $L1_2$  between two  $L1_0$  domains. We have then calculated the en-

ergies of the two  $L1_0/L1_2$  interfaces. All the possibilities for the  $L1_2$  variant and for the position of the APB have been investigated. Only a few examples are shown in Fig. 11. It is easy to find a lower bound for the excess energy. Indeed, each  $L1_2/L1_0$  interface induces an energy cost of at least  $-J_2$  per site of a (110) plane parallel to the APB. The total energy of an APB is then higher than  $-2J_2$ . A complete enumeration of the different configurations shows that this minimum is attained for a single configuration. An example of such a configuration is shown in Fig. 11(a), where it can be seen that the cubic planes formed by the majority atoms of the  $L1_2$  structure belong to the neighboring  $L1_0$  domains [see the dashed lines in Fig. 11(a)]. In other words, using the 3D LRO parameter formalism, our study proves that the lowest-energy configuration at 0 K is obtained when the scalar product of the LRO parameter of the  $L1_2$  layer with that of the neighboring  $L1_0$  domains is positive. This result is in full agreement with our experimental observations of the ODW's in the Co-Pt system. Finally, we have checked that the above result still holds when the interfaces are oriented in a cubic plane.

### B. Finite temperature

To investigate the wetting behavior of ODW's at finite temperature, we use the inhomogeneous CVM-TO described in Sec. IV B. We have selected the temperature  $T = 2.88J_1/k_B$  which is well below the triple point and the ordering spinodal. The chemical potential is  $h = 2.5553922J_1$  to be exactly on the  $L1_0+L1_2$  coexistence line.

As explained above, our inhomogeneous CVM program only deals with flat interfaces parallel to a cubic plane, and [100] conveniently denotes the direction normal to the interfaces. Using the symmetry of the  $L1_0$  structure, we have to consider only two inequivalent ODW's, where the LRO parameters of the bulk domains are either [100][001] (ODW of the first kind) or [010][001] (ODW of the second kind).

The calculation starts with a flat and abrupt ODW parallel to a (100) plane between two  $L1_0$  domains. For the two kinds of ODW's, the minimization of the grand-canonical free energy leads to the splitting of the ODW into two interfaces with a  $L1_2$  layer in between. This result proves that the wetting of the ODW by the  $L1_2$  structure is energetically favored. The LRO parameter of the  $L1_2$  structure is along [111]. It means that the selected  $L1_2$  variant is the one characterized by a positive scalar product with the LRO parameters of the  $L1_0$  bulk domains. This result is in agreement with our experimental observation in the Co-Pt system and consistent with the results obtained at  $T=0$  K. The equilibrium profile obtained at  $T=2.88J_1/k_B$  for the first kind of ODW is presented in Fig. 12.

Note that the two  $L1_0/L1_2$  interfaces are not equivalent, as seen in Fig. 12. Indeed, two components of the LRO parameter are equal across the left-hand side interface, which is not the case for the other interface. This is due to the symmetry invariance of the left-hand-side interface with respect to the (011) plane. In the concentration-wave formalism [see Eq. (2)], this symmetry operation is equivalent to the ex-

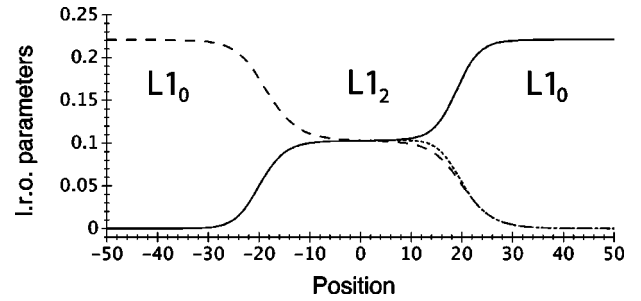


FIG. 12. LRO parameter profile across a wetted ODW of the first kind at  $T=2.88J_1/k_B$ . The fourfold axis of the right- and left-hand-side  $L1_0$  domains are [001] and [100], respectively. Positions are given in lattice parameters of the underlying fcc lattice.

change  $\eta_2 \leftrightarrow \eta_3$ . On the contrary, for the right-hand-side interface, even if the bulk domains remain unchanged by application of the symmetry with respect to the (110) plane, the [100] direction of the normal to the interface is changed. Therefore, the (110) plane is not a symmetry plane for the right-hand-side interface. This qualitative difference between the two interfaces is a sign of the anisotropy of the  $L1_2/L1_0$  interfaces in our model. This anisotropy can be estimated using the energies given in Table III. The  $L1_2/L1_0$  interfacial energy is  $9.8240 \times 10^{-3}J_1$  for the left-hand-side interface, which is more than 8% above the energy of the right-hand-side interface ( $8.9785 \times 10^{-3}J_1$ ). We have not studied in further details the anisotropy of the interfaces in our system. A very convenient approach to do so would be to use a Ginzburg-Landau formalism (see, for example, Refs. 11 and 23).

### C. Triple point

We have seen that along the  $L1_0+L1_2$  coexistence line, the ODW's are wetted by the  $L1_2$  structure at  $T = 2.88J_1/k_B$ . We now examine if this wetting phenomenon persists up to the triple point. As we will see, our calculations show that the wetting behavior of the ODW's is qualitatively different when considering the first or second kind of ODW. In other words, the wetting behavior of ODW's at the triple point is sensitive to the orientation of the interface.

The relaxed profile obtained for the ODW of the first kind is shown in Fig. 13. It is clear that a large layer of  $L1_2$  structure with a LRO parameter along [111] was formed during the minimization procedure. This result suggests that the equilibrium configuration is a macroscopic wetting of the interface by the  $L1_2$  structure. To confirm this point we have to compare the energy obtained at the end of the minimization procedure ( $\Delta F = 7.1296 \times 10^{-3}J_1$ ), to the sum of the two individual  $L1_0/L1_2$  interface energies. Using Table III, the energy of a macroscopic wetting by the  $L1_2$  structure ( $\Delta F = 7.099 \times 10^{-3}J_1$ ) is confirmed to be the most stable configuration. It means that, along the  $L1_0+L1_2$  coexistence line, the wetting of the first kind of ODW by the  $L1_2$  structure persists up to the triple point. Finally, note that the LRO parameter of the  $L1_2$  structure is very small at the triple point ( $\eta = 0.03128$ ), meaning that the  $L1_2$ /fcc phase transition is only weakly of the first order.

TABLE III. Equilibrium structures and energies of flat interfaces normal to the [100] direction. The first column indicates the direction of the LRO parameters of the two bulk domains before the energy minimization. Energies are given in  $J_1$  units per site of a (100) plane.

LRO	$T=2.88J_1/k_B$		$T=T_c$	
	Structure	Energy	Structure	Energy
001/100	$L1_0/L1_2/L1_0$	$1.8802 \times 10^{-2}$	$L1_0/L1_2/L1_0$	$7.100 \times 10^{-3}$
001/00 $\bar{1}$	$L1_0/L1_2/L1_0/L1_2/L1_0$	$3.5914 \times 10^{-2}$	$L1_0/fcc/L1_0$	$4.758 \times 10^{-3}$
100/ $\bar{1}00$	$L1_0/L1_2/L1_0/L1_2/L1_0$	$3.7605 \times 10^{-2}$	$L1_0/L1_2/fcc/L1_2/L1_0$	$9.859 \times 10^{-3}$
111/100	$L1_2/L1_0$	$9.8240 \times 10^{-3}$	$L1_2/L1_0$	$4.706 \times 10^{-3}$
111/001	$L1_2/L1_0$	$8.9785 \times 10^{-3}$	$L1_2/L1_0$	$2.393 \times 10^{-3}$
111/ $\bar{1}00$	$L1_2/L1_0/L1_2/L1_0$	$2.7781 \times 10^{-2}$	$L1_2/fcc/L1_2/L1_0$	$5.153 \times 10^{-3}$
111/00 $\bar{1}$	$L1_2/L1_2/L1_0$	$2.6939 \times 10^{-2}$	$L1_2/fcc/L1_0$	$2.601 \times 10^{-3}$
111/ $\bar{1}\bar{1}\bar{1}$	$L1_2/L1_2$	$1.7961 \times 10^{-2}$	$L1_2/L1_2$	$3.978 \times 10^{-4}$
111/ $\bar{1}\bar{1}1$	$L1_2/L1_0/L1_2$	$1.7957 \times 10^{-2}$	$L1_2/fcc/L1_2$	$4.468 \times 10^{-4}$
000/111			$fcc/L1_2$	$2.234 \times 10^{-4}$
000/100			$fcc/L1_2/L1_0$	$4.929 \times 10^{-3}$
000/001			$fcc/L1_0$	$2.379 \times 10^{-3}$

The wetting behavior of the second kind of ODW can be obtained by comparing the interfacial energies shown in Table III. The energy of a macroscopic wetting by the  $L1_2$  structure—i.e., the 010/111/001 LRO parameter profile—is small ( $4.786 \times 10^{-3} J_1$ ). However, the energy of a macroscopic wetting by the fcc solid solution is a little less ( $4.758 \times 10^{-3} J_1$ ). We conclude that the wetting of the second kind of ODW qualitatively changes between  $T = 2.88 J_1/k_B$  and  $T = T_c$ . We thus predict the existence of a transition temperature, below which complete wetting by the  $L1_2$  structure is favored. Above this transition temperature, the ODW is only partially wetted by the disordered phase, and the width of the interface diverges when reaching  $T_c$ . At the triple point a macroscopic wetting by the fcc solid solution is thus predicted. However, considering the very small energy difference between the wetting profiles at  $T_c$  ( $L1_2$  or fcc) we suspect that the transition temperature may be too close to  $T_c$  to be experimentally observed.

## VI. WETTING OF NONCONSERVATIVE APB'S

We now consider the equilibrium structure of APB's in the  $L1_0$  structure. For simplicity, we focus on APB's parallel

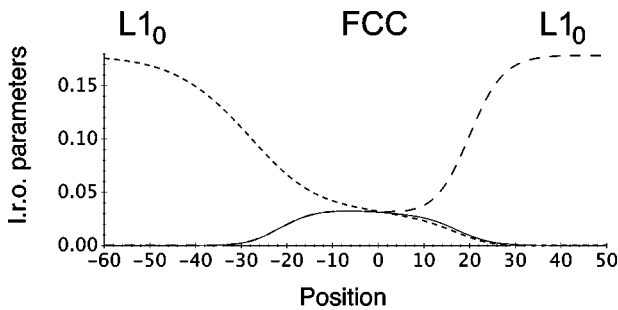


FIG. 13. LRO parameter profile across a wetted ODW at  $T_c$ . Positions are given in lattice parameters of the underlying fcc lattice.

to cubic planes. Depending on the orientation of the fourfold axis of the  $L1_0$  domains, two kinds of APB's have to be distinguished. The APB is called a “nonconservative APB” when the fourfold axis is perpendicular to the interface because an excess concentration is created at the interface [see Fig. 14(b)]. On the other hand, the APB is called a “conservative APB” when the fourfold axis is contained in the interface plane [see Fig. 14(a)]. The present section is devoted to the wetting behavior of the nonconservative APB. Conservative APB's will be studied in Sec. VII.

## A. Introduction

The wetting of nonconservative APB's in the  $L1_0$  structure by the *disordered fcc solid solution* has been studied by Mazaurec and Nasu<sup>4,36</sup> using a microscopic model with interactions limited to first nearest neighbors. Using the CVM in the tetrahedron approximation, the authors show that the equilibrium profile is very sensitive to the temperature. At low enough temperature, the nonconservative APB's dissociate and a new  $L1_0$  layer is formed. Above a critical temperature (prewetting temperature) the equilibrium structure of the APB is a direct profile between the  $L1_0$  bulk domains. Finally, as the temperature increases up to the bulk  $L1_0/fcc$  transition, a complete wetting by the fcc solid solution of the nonconservative APB is observed.

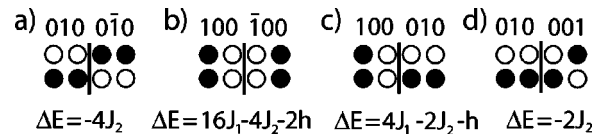


FIG. 14. Interfacial energies at 0 K in the  $L1_0$  structure in a second nearest-neighbor interaction model: (a) conservative APB, (b) nonconservative APB, (c) ODW of the first kind, and (d) ODW of the second kind. The LRO parameters of the  $L1_0$  domains are indicated above. Energies are given per site of a (100) plane parallel to the interface.



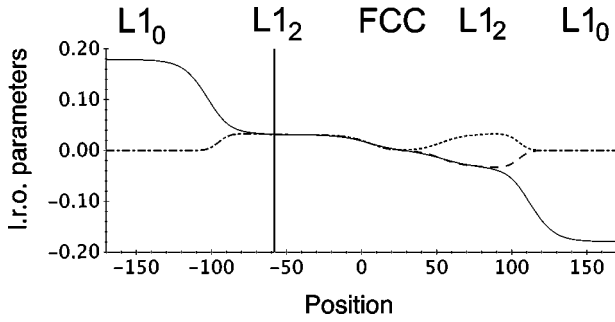


FIG. 17. Wetting of a nonconservative APB in the  $L1_0$  structure when  $T=T_c$ . As noted by the vertical line, the LRO parameter profile shown here has been obtained by the concatenation of two independent calculation boxes.

ize the transition between these two regimes. To do so, it is sufficient to study the three inner layers—i.e., the wetting behavior of an antiphase boundary between two  $L1_2$  domains. For a given nonconservative APB in the  $L1_0$  phase and in the case of a wetting by a sequence  $L1_2/L1_0/L1_2$ , four equivalent possibilities exist for the middle  $L1_0$  layer. Only one of these need to be considered. To simplify the notation, we consider in the following that the equilibrium LRO parameter profiles is the one drawn in Fig. 15—i.e.,  $100/111/010/\bar{1}\bar{1}/\bar{1}00$ . In other words, we have to study the wetting behavior of the APB in the  $L1_2$  structure between two bulk domains characterized by the LRO parameters  $111$  and  $\bar{1}\bar{1}\bar{1}$ .

The wetting of APB in the  $L1_2$  phase by the  $L1_0$  structure has already been studied experimentally in the Co-Pt system.<sup>11</sup> Near the  $L1_2+L1_0$  two-phase stability region, APB's in the  $L1_2$  structure are wetted by a layer of  $L1_0$  structure, and the LRO parameter characterizing the new  $L1_0$  structure is situated in the middle of the LRO parameters of the two  $L1_2$  bulk domains. Then the authors developed different theoretical approaches based on the Ising model.<sup>11</sup> Using a mean-field approximation, their model was able to predict the wetting of the APB in the  $L1_2$  phase by the same  $L1_0$  variant as observed experimentally. However, because the topology of the mean-field phase diagram is inaccurate, the authors were unable to investigate the wetting behavior of APB in the  $L1_2$  phase near the triple point.

As already mentioned, the CVM-TO correctly predicts a triple point at finite temperature (see Fig. 10). We have thus been able to study the wetting behavior of the APB in the  $L1_2$  phase up to the triple point. As can be guessed from Figs. 16 and 17, the APB between the two bulk domains characterized by the LRO parameters  $111$  and  $\bar{1}\bar{1}\bar{1}$  is wetted by the  $L1_0$  structure at  $T=2.88J_1/k_B$  and wetted by the fcc solid solution at the triple point. We have studied the transition between these two regimes by comparing the configuration obtained after relaxation of a sharp APB and the wetting by the  $L1_0$  structure. First, we have found that above  $T=2.9717J_1/k_B$  the relaxation of the sharp APB leads to a LRO parameter profile with a finite thickness (see Fig. 18). For convenience, we call this profile the dewetted configuration. The thickness of the profile increases with increasing

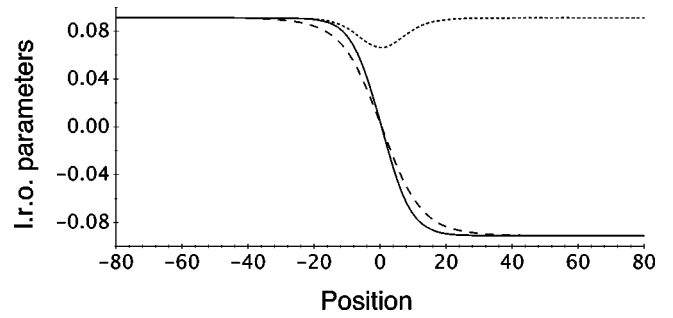


FIG. 18. Evolution of the LRO parameters across a nonconservative APB in the  $L1_2$  structure at  $T=2.985J_1/k_B$ .

temperature and finally diverges when reaching the triple point where the wetting by the fcc solid solution is the equilibrium configuration.

To determine whether the dewetted profile is the equilibrium one, we have compared the energy obtained after relaxation with that of a perfect wetting by the  $L1_0$  structure—i.e., with twice the  $L1_0/L1_2$  interfacial energy. The result, presented in Fig. 19, shows clearly the existence of a transition temperature close to  $T=2.971734J_1/k_B$  below which the wetting by the  $L1_0$  is the equilibrium configuration and above which the dewetted profile is favored. The crossing of the two curves indicates that the transition is of the first order. Note that, when  $J_2/J_1=-0.2$ , this dewetting temperature is only 1% below the triple-point temperature. A detailed study of the influence of the choice of  $J_2/J_1$  on the value of the transition temperature would be important to test the generality of this phenomenon.

## F. Conclusion

Our calculations both at  $T=0$  K and at finite temperature indicate that, if we are not too close to the triple point, the nonconservative APB's in the  $L1_0$  structure are wetted by three layers  $L1_2/L1_0/L1_2$ . In other words, the APB splits into two ODW's which are both wetted by the  $L1_2$  structure. This point is consistent with our observations in the Co-Pt system (see Figs. 5 and 8). Above the critical temperature

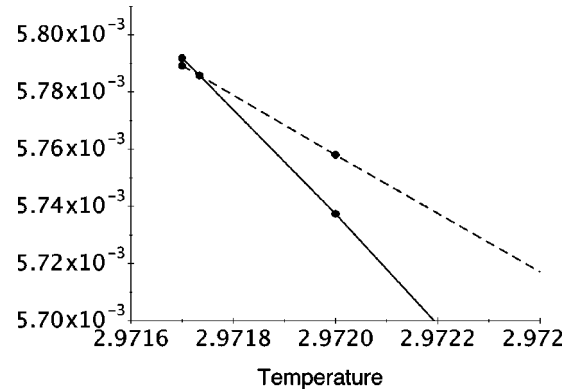


FIG. 19. Measurement of the dewetting temperature of the nonconservative APB in the  $L1_2$  structure. The solid line is the energy of the dewetted profile ( $L1_2/L1_2$ ) and the dashed line is twice the  $L1_2/L1_0$  interfacial energy.

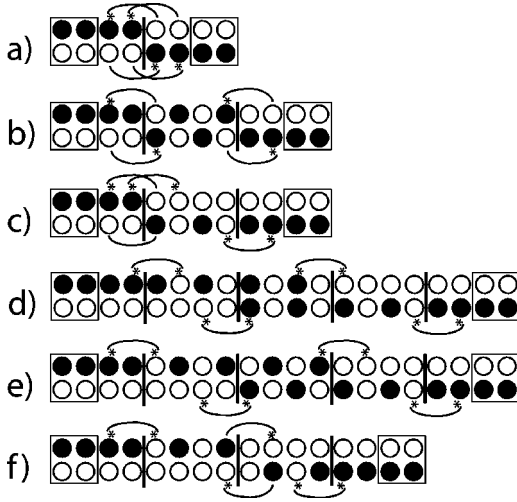


FIG. 20. Equilibrium structures at 0 K of the conservative APB in the  $L1_0$  structure with a second nearest-neighbor interaction model. The rounded curves point out the unfavorable second nearest-neighbor pair responsible for the interfacial energies. The exited states of lowest energy are obtained by changing the chemical nature of one of the atoms designated by an asterisk (see text for explanation).

$T = 2.971734J_1/k_B$ , our CVM-TO calculations predict that the equilibrium profile of the nonconservative APB in the  $L1_0$  structure is a wetting by two  $L1_2$  layers. The LRO parameter profile between these two  $L1_2$  layers has a finite thickness which increases with increasing temperature and finally diverges when reaching the triple point. Therefore, at the triple point, the nonconservative APB in the  $L1_0$  structure is wetted by the three layers  $L1_2/fcc/L1_2$ .

## VII. WETTING OF CONSERVATIVE APB'S

We now consider the equilibrium structure of the conservative APB's in the  $L1_0$  structure; i.e., we only consider APB's which are parallel to a cubic plane and where the fourfold axis of the bulk domains is contained in the interface plane [see Fig. 20(a)].

### A. $T = 0$ K

With our second nearest-neighbor interaction model, the ground state of the conservative APB in the  $L1_0$  structure is degenerate when  $h = 4J_1$ —i.e., when the  $L1_0$  and  $L1_2$  structures are simultaneously stable. Indeed, we have found six qualitatively different profiles associated with the lowest energy. This interfacial energy is  $-4J_2$  per site of a (100) plane parallel to the APB and is then equal to the ground-state energy of the nonconservative APB. The six ground-state configurations are drawn in Fig. 20 where the unfavorable second nearest-neighbor pair responsible for the interfacial energy are pointed out.

### B. Low-temperature expansion

We introduced above a low-temperature analysis of the phase diagram to analyze the competition between the bulk

$L1_0$  and  $L1_2$  phases. Now, we can use the same approach to investigate the equilibrium configuration of an interface when the interface ground state is degenerated at  $T = 0$  K and  $h = h_c$ .

To compare the relative stabilities at finite temperature of these ground-state configurations, we first have to determine the lowest excitation energy  $\Delta E'_{n_0}$  whose degeneracies  $\mu_{n_0}^i$  are not the same in the different configurations. According to Eq. (10), the free energy difference between two ground-state configurations 1 and 2 will then be given by, to the lowest order in  $kT$ ,

$$F_2(h, T) - F_1(h, T) = E_2(h) - E_1(h) - kT(\mu_{n_0}^2 - \mu_{n_0}^1) \times \exp(-\beta \Delta E'_{n_0}), \quad (13)$$

where the free energy  $F_i$ , the internal energy  $E_i$ , and the degeneracy  $\mu_{n_0}^i$  are expressed per site of a plane parallel to the interface. Of course, if  $h$  is kept fixed at  $h_c$ , Eq. (13) tells us that, at low enough temperature, the equilibrium interface configuration corresponds simply to the one with the highest number of excitations of energy  $\Delta E'_{n_0}$ .

In the present situation, we want to analyze the interface configuration along the  $L1_0/L1_2$  equilibrium line: the internal energy differences  $E_2(h) - E_1(h)$  do not vanish anymore. Therefore, we need to estimate the free energy differences when the chemical potential  $h$  is related to the temperature  $T$  by Eq. (12). In Eq. (12), the temperature dependence of  $h$  is linked to the lowest excitation energy  $\Delta E_{n_0}$ , which differentiates the two bulk phases. As we will see next, the lowest excitation energy  $\Delta E'_{n_0}$  that separates the interface configurations is smaller than  $\Delta E_{n_0}$ . As a consequence, the temperature dependence of the chemical potential  $h(T)$  can be neglected in Eq. (13) and we finally get, to the lowest order in  $kT$ ,

$$F_2(h(T), T) - F_1(h(T), T) = -kT(\mu_{n_0}^2 - \mu_{n_0}^1) \exp(-\beta \Delta E'_{n_0}). \quad (14)$$

As a result, at finite but low enough temperature, *even along the  $L1_0/L1_2$  equilibrium line*, the equilibrium configuration of the interface is still the ground-state configuration associated with the highest degeneracy of the lowest-energy excitation.

We now proceed to the identification of  $\Delta E'_{n_0}$ . As can be seen in Fig. 20, all the ground-state configurations can be obtained by the formation of one or several  $L1_2$  or  $L1_0$  layers between the two bulk domains. As we consider only the situation along the  $L1_0/L1_2$  equilibrium line, we may suppose that the widths of these layers are infinite [more precisely, provided that each layer involves at least four (100) planes, the competition between the configurations does not depend on the respective lengths of the intermediate layers]. By studying the configurations sketched in Fig. 20, we have found that the lowest excitation energy is  $\Delta E'_{n_0} = -8J_2$  and that the exited states of lowest energy are obtained by changing the chemical nature of one of the atoms designated by an

asterisk in Fig. 20. We first note that, as announced above,  $\Delta E'_{n_0}$  is smaller than the lowest bulk excitation energy. Therefore, the competition between the different interfaces is indeed governed by Eq. (14). Second, it is clear that the degeneracy of  $\Delta E'_{n_0}$  is maximum for the configurations  $d$  and  $e$ :  $\mu_{n_0}^d = \mu_{n_0}^e = 8$ . Using Eq. (14), we conclude that at low but finite temperature, the most stable configuration is necessarily  $d$  or  $e$ . It implies that the most stable configuration is a wetting by three new layers  $L1_2/L1_0/L1_2$ . This result, which is similar to that obtained for the nonconservative APB, is in agreement with the experimental observations in the Co-Pt system.

We would like to emphasize that this result is highly non-trivial: the most stable configuration is also one of the most complex ones, as it consists of a sequence of four consecutive interfaces. It is also worth pointing out that a simple  $J_1 - J_2$  model does reproduce this complexity.

Finally, we mention that with our low temperature expansion, even when considering the higher-order excitation energies  $-12J_2$ , we were not able to differentiate the free energies of the configurations  $d$  and  $e$ . Note that, next to the  $d$  and  $e$  configurations, the most stable one is  $f$ —i.e., a wetting by two  $L1_2$  layers. As we will see next using a CVM analysis, this configuration becomes the most stable one at higher temperature. In this respect, we report in the Appendix a detailed analysis of the excess interface free energies of configurations  $e$  and  $f$  along the equilibrium line, up to the next lowest excitation energy ( $-12J_2$ ) (this is required if we want to take into account the temperature dependence of  $h$  along the equilibrium line).

### C. Finite temperature

To determine the equilibrium profile of the conservative APB at higher temperature, we have performed CVM-TO calculations at  $T = 2.88J_1/k_B$ . Using the interfacial energies gathered in Table III, we predict that the equilibrium configuration is a wetting by three layers  $L1_2/L1_0/L1_2$ , where the tetragonal axis of the new  $L1_0$  layer is parallel to the interface plane (configuration  $e$  in Fig. 20). The corresponding LRO profile is presented in Fig. 21. This result is consistent with our low-temperature expansion presented above. However, at  $T = 2.88J_1/k_B$  we predict that the interfacial energy of configuration  $d$  is higher than the one of configuration  $e$ :  $F_d - F_e = 1.69 \times 10^{-3}J_1$  per site of a (100) plane parallel to the interface.

At  $T = 2.88J_1/k_B$ , the interfacial free energy of the configuration  $f$  is only slightly above that of the configuration  $e$ :  $F_f - F_e = 4 \times 10^{-6}J_1$ . We may therefore suspect that at a higher temperature, the configuration  $f$  may become the most stable configuration. We have confirmed this point by computing the interfacial energies at a higher temperature. When  $T = 2.971734J_1/k_B$  (and  $h = 1.9799713J_1$ ), our CVM-TO calculations show that the free energy difference  $F_f - F_e$  is equal to  $-2.39 \times 10^{-3}J_1$ , implying that the configuration  $f$  becomes the most stable configuration for the conservative APB. We have not tried to obtain a precise value for the transition temperature  $T_{e/f}$  between the low-temperature sta-

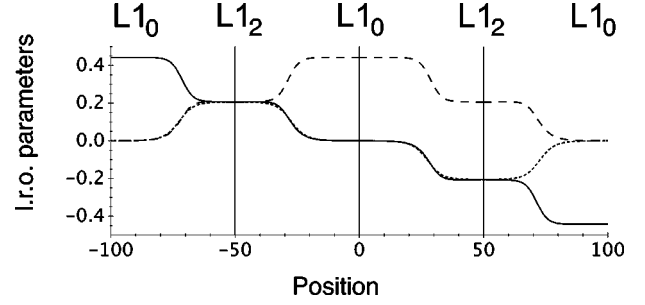


FIG. 21. Wetting of a conservative APB in the  $L1_0$  structure when  $T = 2.88J_1/k_B$ . Positions are given in lattice parameters of the underlying fcc lattice. The LRO parameter goes from  $00\bar{1}$  to  $001$ . As noted by the vertical lines, the LRO parameter profile shown here has been obtained by the concatenation of four independent calculation boxes.

bility region of the configuration  $e$  and the high-temperature stability region of the configuration  $f$ . However, given the extremely low value of  $F_f - F_e$  at  $T = 2.88J_1/k_B$ , we expect that  $T_{e/f}$  is only slightly above  $T = 2.88J_1/k_B$ .

### D. Triple point

At the triple point, using the interfacial energies gathered in the Table III, we conclude that the equilibrium configuration of the  $L1_0/L1_0$  conservative APB is a wetting by the disordered solid solution. The corresponding LRO profile is shown in Fig. 22. Moreover, our CVM-TO calculations show that the configuration  $f$  (which is the equilibrium configuration at  $T = 2.971734J_1/k_B$ ) is metastable at the triple point. The transition between these two configurations is thus of first order. We did not try to determine neither the value of this transition temperature nor its evolution with the range and value of the interaction energies of our model.

Note that the metastability of the configuration  $f$  at the triple point is a direct consequence of the stability of the conservative APB in the  $L1_2$  structure. In other words, the conservative APB's in the  $L1_2$  structure are not wetted at the

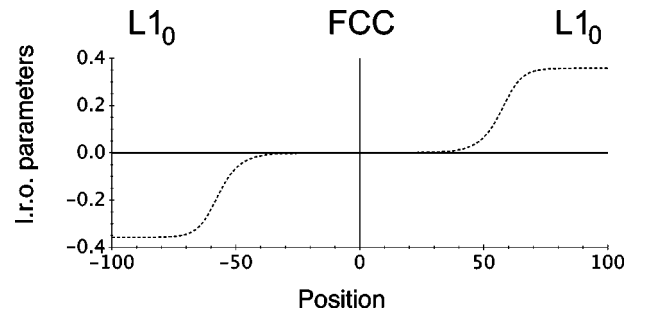


FIG. 22. Wetting of a conservative APB in the  $L1_0$  structure when  $T = T_c$ . Positions are given in lattice parameters of the underlying fcc lattice. The LRO parameter goes from  $00\bar{1}$  to  $001$ . The first and second components of the LRO parameters are zero. As noted by the vertical line, the LRO parameter profile shown here has been obtained by the concatenation of two independent calculation boxes.

triple point. This result illustrates the fact that the wetting is not unavoidable when the relevant order parameter is multi-dimensional.

### E. Conclusion

As a conclusion, when increasing the temperature along the  $L1_2/L1_0$  coexistence line, we predict the following evolution for the equilibrium configuration of the conservative APB in the  $L1_0$  structure. At low temperature, the conservative APB is wetted by three layers  $L1_2/L1_0/L1_2$ , where the tetragonal axis of the new  $L1_0$  layer is parallel to the interface plane (configuration  $e$  in Fig. 20). We recall that this nontrivial result has been obtained with two different methods (low-temperature expansion and CVM analysis) based on the simplest Ising model. All together, this emphasizes the generic aspects of this complex situation.

We also analyzed the situation close to the triple point. At a temperature slightly above  $T=2.88J_1/k_B$ , the equilibrium structure of the conservative APB in the  $L1_0$  structure becomes a wetting by two  $L1_2$  layers separated by a conservative APB (configuration  $f$  in Fig. 20). Finally, below the triple-point temperature, we predict a first-order transition between the  $f$  configuration and a direct profile between the two  $L1_0$  bulk domains. The width of this profile is finite, but diverges when reaching the triple point where a perfect wetting by the disordered solid solution is obtained.

## VIII. SUMMARY AND CONCLUSION

The present paper supplements and enlarges the previous results obtained on the wetting phenomenon of interfaces in ordered alloys during solid-solid phase transformations.<sup>1-4,6-8,11</sup> Most studies were dedicated to the wetting of interfaces by the disordered solid solution. In the present paper, we studied the wetting by an *ordered* phase, where new features are expected because of the degeneracy of the ordered structure. More precisely, we studied the behavior of interfaces in a  $L1_0$  sample with a composition close to  $\text{Co}_{40}\text{Pt}_{60}$ . Due to the topology of the Co-Pt phase diagram, a simple cooling experiment drives the  $L1_0$  sample near the  $L1_0+L1_2$  two-phase stability region, and we thus expect the formation of  $L1_2$  phase in the sample. Using different transmission electron microscopy techniques, we showed that, indeed, the above thermal treatment leads to the formation of  $L1_2$  layers along the  $L1_0/L1_0$  interfaces. However, ODW's and APB's behave very differently: ODW's are wetted by a single layer of  $L1_2$  whereas the wetting of APB's leads to the formation of three new macroscopic layers  $L1_2/L1_0/L1_2$ . This behavior is most surprising because the wetted APB contains four consecutive  $L1_0/L1_2$  interfaces, which seems, at first sight, an unfavorable configuration in comparison to a single  $L1_0/L1_0$  interface.

To explain this peculiar phenomenon, we used an Ising model with interactions limited to first and second nearest-neighbor atoms. This approach is generic in the sense that it is the simplest one that reproduces the observed  $L1_0$  and  $L1_2$  ground states, without the specificities of the model with first nearest-neighbor interactions only. To investigate the behav-

ior of interfaces from  $T=0$  K up to the triple-point temperature, we first analyzed the interface ground states, and we used two different finite-temperature techniques: low-temperature expansions and the inhomogeneous cluster variation method in the tetrahedron-octahedron approximation. The results of all these approaches are in agreement with our experimental observations in the Co-Pt system when considering the wetting of both ODW's and APB's. We point out that the complexity of the observed wetting phenomena, in particular the wetting of APB's with three macroscopic layers, is explained using a very simple model on a rigid lattice, with pair interactions limited to second nearest-neighbors atoms.

It is, however, important to test the validity of our results when increasing the range of the interaction energies. If we consider small interaction energies  $J_3$  and  $J_4$  between third and fourth nearest-neighbor atoms, preliminary results show that only the value of  $J_3$  can change the relative stability of the relevant interface configurations. For example, when considering the conservative APB in the  $L1_0$  phase,  $J_3$  lifts the degeneracy of the ground-state configurations detailed in Fig. 20 for a model limited to  $J_1$  and  $J_2$ . In particular, when  $J_3>0$ , the ground-state configuration is similar to the experimental observations, with the formation of the three layers  $L1_2/L1_0/L1_2$ .

It would also be very interesting to model interfaces with arbitrary orientations that are not flat. This could be done relatively easily through Monte Carlo (MC) simulations. However, as discussed in the paper, the free energy differences involved here in the competition between the different interface configurations are extremely small and out of reach of the precision that MC simulations can afford. This is why we opted for a closed-form formalism (the CVM), which is, from the numerical point of view, very precise even for inhomogeneous configurations. Unfortunately, the price to pay is that we need to reduce the dimensionality of the problem in order to decrease the number of variational parameters. In other words, we had to restrict the interface to a simple crystallographic orientation. In particular, we did not take into account the possible atomic ledges along the interfaces. Moreover, we chose the (100) orientation, whereas the experimental interfaces are very close to (110) planes. Even though these are not the same, the calculated interface configurations present the same sequence of layers as the observed one. This shows that the results are generic and robust and justifies the calculation modeling.

The CVM calculation results obtained in the present study illustrate the complexity of the wetting phenomena when, as is the case here, the relevant LRO parameter is multidimensional and the equilibrium structures are ordered. Indeed, we have observed situations where wetting of interfaces does not occur (e.g., for conservative  $L1_2/L1_2$  APB's) and situations where several macroscopic layers are formed simultaneously (e.g., for  $L1_0/L1_0$  APB's). Moreover, our calculations near the triple point show that the wetting behavior of a given interface may change *qualitatively* with its orientation. For example, conservative APB's in the  $L1_0$  structure at the triple point are wetted by the disordered solid solution when they are in a conservative orientation and by three layers

$L1_2/fcc/L1_2$  in a nonconservative orientation.

Note also that, when increasing the temperature along the  $L1_0/L1_2$  coexistence line, the wetting behavior of an interface may change, as is clearly illustrated with the nonconserved APB in the  $L1_0$  structure. Indeed, from 0 K up to the triple point, we observe the following successive equilibrium structures for the APB:  $L1_0/L1_2/L1_0/L1_2/L1_0$ ,  $L1_0/L1_2/L1_2/L1_0$ ,  $L1_0/L1_0$ , and then finally  $L1_0/fcc/L1_0$ . We also emphasize that we have been able to study the wetting phenomenon of interfaces up to the disordered phase because the CVM-TO predicts a correct topology of the phase diagram with a triple point at finite temperature. However, the position of the triple point may not be correctly reproduced. This has been discussed in the literature when the interactions are limited to the first neighbors only (see, for example, Refs. 28 and 41). Therefore, the transitions observed close to  $T_c$  may be sensitive to the thermodynamical model and to the value of the interaction energies. In that respect, the results obtained with our CVM calculations at the triple point may be less generic than the ones predicted at lower temperature, using simultaneously low-temperature expansions and CVM calculations.

Finally, we would like to point out that our theoretical model does not take into account the elastic energy that appears during the coherent coexistence of structures differing in symmetry and lattice parameters, as is the case with  $L1_0$  and  $L1_2$  structures. It proves that the complex wetting phenomenon of APB's in the  $L1_0$  structure is due to the short-range chemical interactions only. More precisely, when considering a flat interface, it is easy to show that the coherency elastic energy is proportional to the width of the wetting layer. Therefore, our theoretical model on a rigid lattice is valid during the initial stage of the wetting phenomenon, when the width of the wetting layer is thin enough so that the elastic energy is negligible in front of the interfacial energies arising from the short-range chemical interactions. At later stages, the competition between elastic and interfacial energies may induce microstructural changes (see, for example, Refs. 12 and 13), but this point is beyond the scope of the present paper.

#### ACKNOWLEDGMENTS

The authors gratefully acknowledge F. Ducastelle for very helpful discussions and thank G. Schmerber, Dr. V. Pierron-Bohnes (University of Strasbourg, France), and D. Regen (ONERA) for their help in preparing the Co-Pt samples.

#### APPENDIX

In this appendix, we present how to determine precisely the low-temperature expression of the free energy difference between two competitive interfaces. As an example, we focus on the configurations labeled  $e$  and  $f$  in Fig. 20. As shown above, the two configurations lead to the same interfacial energy  $-4J_2$  per site of a (100) plane and have the same lowest excitation energy is  $\Delta E'_{n_0} = -8J_2$ . We recall that we want to express this free energy difference in the wetting regime—i.e., along the  $L1_0/L1_2$  equilibrium line. In

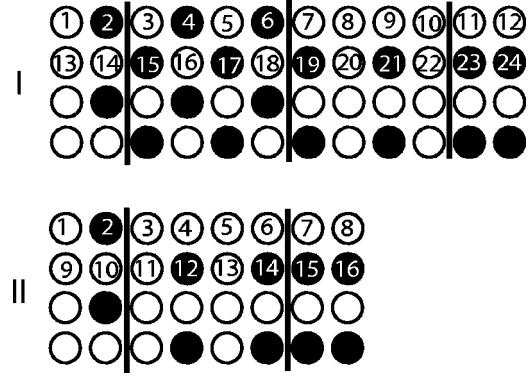


FIG. 23. Configurations I and II and the labeling of each site. Configurations I and II correspond to the configurations  $e$  and  $f$  in Fig. 15.

this appendix, we show how to perform the low-temperature expansion up to the order  $\exp(-12\beta J_2)$ —i.e., beyond the contribution of the lowest excitation energy  $\Delta E'_{n_0} = -8J_2$ .

Because we are interested in the free energy difference between the configurations  $e$  and  $f$ , we only need to consider the sites which differ between the two configurations. These sites, listed in Fig. 23, are labeled I and II for the configurations  $e$  and  $f$ , respectively. The corresponding single-spin-flip excitation energies are detailed in Table IV.

Obviously, all the single-spin-flip excitation energies  $\Delta E = -8J_2$  and  $\Delta E = -12J_2$  should enter our analysis. It is clear that there is no other excitation of energy  $\Delta E = -8J_2$  than those displayed in Table IV. However, it is not so simple for the excitation energy  $\Delta E = -12J_2$ , because there are connected clusters whose excitation energies are also equal to  $\Delta E = -12J_2$ . Indeed, these clusters are all the second nearest-neighbor pairs parallel to the interfaces and whose sites have an excitation energy equal to  $\Delta E = -8J_2$  (the excitation energy of a pair  $n, m$  is given by  $\Delta E_{nm} = \Delta E_n + \Delta E_m + 4J_{nm}\sigma_n\sigma_m$ , where the  $\Delta E_n$  and  $\Delta E_m$  are the spin-flip interaction energies of site  $n$  and  $m$  and  $J_{nm}$  the interaction between the sites). This involves the second nearest-neighbor pair parallel to the interface that originate from sites 6,8,13,15,22,24 in configuration  $e$  and from sites 4,10,13,15 in configuration  $f$ . It is easy to convince oneself that all other clusters have excitation energies larger than  $\Delta E = -12J_2$ .

Finally, using Eq. (9), a simple counting of the information collected in Table IV, together with the incorporation of the second nearest-neighbor pairs that we have just identified, leads to the following excess free energy expansions per site of the (100) plane:

$$\begin{aligned} \Delta \mathcal{F}_I(h(T), T) = & \frac{1}{2} \{ -6h(T) - 24J_1 + 66J_2 - 6kT \exp(8\beta J_2) \\ & - 18kT \exp(12\beta J_2) - 24F_{eq}(T) \} \\ & + O(\exp(16\beta J_2)), \end{aligned} \quad (A1)$$

$$\begin{aligned} \Delta \mathcal{F}_{II}(h(T), T) = & \frac{1}{2} \{ -6h(T) - 8J_1 + 42J_2 - 4kT \exp(8\beta J_2) \\ & - 14kT \exp(12\beta J_2) - 16F_{eq}(T) \} \\ & + O(\exp(16\beta J_2)), \end{aligned} \quad (A2)$$

TABLE IV. Energy increase  $\Delta E$  when flipping the site occupancy and contribution to the ground-state energy per site,  $E_{g.s.}$ , of each site of configurations I and II. The site labeling is presented in Fig. 23.

Site	Configuration I		Configuration II	
	$E_{g.s.}$	$\Delta E$	$E_{g.s.}$	$\Delta E$
1	$-h+2J_1+3J_2$	$0J_1-12J_2$	$-h+2J_1+3J_2$	$0J_1-12J_2$
2	$+h-4J_1+3J_2$	$8J_1-12J_2$	$+h-6J_1+2J_2$	$16J_1-8J_2$
3	$-h-2J_1+3J_2$	$16J_1-12J_2$	$-h+2J_1+3J_2$	$0J_1-12J_2$
4	$+h-2J_1+3J_2$	$0J_1-12J_2$	$-h+2J_1+2J_2$	$0J_1-8J_2$
5	$-h-2J_1+3J_2$	$16J_1-12J_2$	$-h+2J_1+3J_2$	$0J_1-12J_2$
6	$+h-2J_1+2J_2$	$0J_1-8J_2$	$-h+0J_1+3J_2$	$8J_1-12J_2$
7	$-h+0J_1+3J_2$	$8J_1-12J_2$	$-h-2J_1+3J_2$	$16J_1-12J_2$
8	$-h+2J_1+2J_2$	$0J_1-8J_2$	$-h-2J_1+3J_2$	$16J_1-12J_2$
9	$-h+2J_1+3J_2$	$0J_1-12J_2$	$-h+2J_1+3J_2$	$0J_1-12J_2$
10	$-h+2J_1+3J_2$	$0J_1-12J_2$	$-h+2J_1+2J_2$	$0J_1-8J_2$
11	$-h+0J_1+3J_2$	$8J_1-12J_2$	$-h+2J_1+3J_2$	$0J_1-12J_2$
12	$-h-2J_1+3J_2$	$16J_1-12J_2$	$+h-6J_1+2J_2$	$16J_1-8J_2$
13	$-h+2J_1+2J_2$	$0J_1-8J_2$	$-h+2J_1+2J_2$	$0J_1-8J_2$
14	$-h+0J_1+3J_2$	$8J_1-12J_2$	$+h-4J_1+3J_2$	$8J_1-12J_2$
15	$+h-2J_1+2J_2$	$0J_1-8J_2$	$+h-2J_1+2J_2$	$0J_1-8J_2$
16	$-h-2J_1+3J_2$	$16J_1-12J_2$	$+h-2J_1+3J_2$	$0J_1-12J_2$
17	$+h-2J_1+3J_2$	$0J_1-12J_2$		
18	$-h-2J_1+3J_2$	$16J_1-12J_2$		
19	$+h-4J_1+3J_2$	$8J_1-12J_2$		
20	$-h+2J_1+3J_2$	$0J_1-12J_2$		
21	$+h-6J_1+3J_2$	$16J_1-12J_2$		
22	$-h+2J_1+2J_2$	$0J_1-8J_2$		
23	$+h-4J_1+3J_2$	$8J_1-12J_2$		
24	$+h-2J_1+2J_2$	$0J_1-8J_2$		

where  $F_{eq}(T)$  is the free energy expansion (per site) up to the order  $\exp(12\beta J_2)$  of either  $L1_0$  or  $L1_2$  along the equilibrium line. Using Eq. (10) and the information displayed in Table II, we easily find that

$$F_{eq}(T) = -2J_1 + 3J_2 - \frac{kT}{2} \exp(12\beta J_2) + O(\exp(16\beta J_2)). \quad (\text{A3})$$

Inserting Eq. (A3) into Eqs. (A1) and (A2), and using the expression of  $h(T)$  given in Eq. (12), we get

$$\Delta \mathcal{F}_I(h(T), T) = -3J_2 - 3kT \exp(8\beta J_2) - \frac{3kT}{2} \exp(12\beta J_2) + O(\exp(16\beta J_2)), \quad (\text{A4})$$

$$\Delta \mathcal{F}_{II}(h(T), T) = -3J_2 - 2kT \exp(8\beta J_2) - \frac{3kT}{2} \exp(12\beta J_2) + O(\exp(16\beta J_2)). \quad (\text{A5})$$

As a result, the excess free energy difference between configurations  $e$  and  $f$  (defined in Fig. 15) is, per site of a (100) plane,

$$\delta \mathcal{F}(h(T), T) = -kT \exp(8\beta J_2) + O(\exp(16\beta J_2)). \quad (\text{A6})$$

Of course, we recover that configuration  $e$  is more stable than configuration  $f$ , as discussed in the text.

<sup>1</sup>R. Kikuchi and J.W. Cahn, *Acta Mater.* **24**, 1337 (1979).

<sup>2</sup>A. Finel, V. Mazauric, and F. Ducastelle, *Phys. Rev. Lett.* **65**, 1016 (1990).

<sup>3</sup>A. Finel, *Ordering and Disorder in Alloys* (Elsevier Applied Science, London, 1992), p. 182.

<sup>4</sup>V. Mazauric, *J. Comput.-Aided Mater. Des.* **4**, 113 (1997).

<sup>5</sup>V.G. Vaks, *JETP Lett.* **76**, 93 (2002).

<sup>6</sup>C. Leroux, *Europhys. Lett.* **12**, 155 (1990).

<sup>7</sup>C. Leroux, A. Loiseau, M.C. Cadeville, D. Broddin, and G. Van Tendeloo, *J. Phys.: Condens. Matter* **2**, 3479 (1990).

<sup>8</sup>C. Ricolleau, A. Loiseau, F. Ducastelle, and R. Caudron, *Phys. Rev. Lett.* **68**, 3591 (1992).

<sup>9</sup>A. Loiseau, *Curr. Opin. Solid State Mater. Sci.* **1**, 369 (1996).

<sup>10</sup>F. Ducastelle, C. Ricolleau, and A. Loiseau, in *Reactive Phase Formation at Interfaces and Diffusion Processes*, edited by Y. Limoge and J. Bocquet (Trans Tech Publications, Aedermanns-

- dorf, 1994), Vols. 155–156, p. 367.
- <sup>11</sup>Y. Le Bouar, A. Loiseau, A. Finel, and F. Ducastelle, *Phys. Rev. B* **61**, 3317 (2000).
- <sup>12</sup>Y. Le Bouar and A. Loiseau, *Acta Mater.* **49**, 2679 (2001).
- <sup>13</sup>Y. Le Bouar and A.G. Khachatryan, *Acta Mater.* **48**, 1705 (2000).
- <sup>14</sup>C. Leroux, A. Loiseau, D. Broddin, and G. Van Tendeloo, *Philos. Mag. B* **64**, 57 (1991).
- <sup>15</sup>C. Leroux, Ph.D. thesis, Université de Strasbourg, France, 1989.
- <sup>16</sup>A. G. Khachatryan, *The Theory of Structural Transformations in Solids* (Wiley, New York, 1983).
- <sup>17</sup>Z.-W. Lai, *Phys. Rev. B* **41**, 9239 (1990).
- <sup>18</sup>F. Ducastelle, *Order and Phase Stability in Alloys* (North-Holland, Amsterdam, 1991).
- <sup>19</sup>P. Stadelmann, *Ultramicroscopy* **21**, 131 (1987).
- <sup>20</sup>A. Roitburd, *Sov. Phys. Solid State* **10**, 2870 (1968).
- <sup>21</sup>A.G. Khachatryan and G. Shatalov, *Sov. Phys. JETP* **29**, 557 (1969).
- <sup>22</sup>Y. Le Bouar, Ph.D. thesis, Ecole Polytechnique, Palaiseau, France, 1998.
- <sup>23</sup>R.J. Braun, J.W. Cahn, G.B.M. Fadden, and A.A. Wheeler, *Philos. Trans. R. Soc. London, Ser. A* **355**, 1787 (1997).
- <sup>24</sup>F. Ducastelle, in *Alloy Phase Stability*, Vol. 163 of NATO Advanced Study Institute, Series E, edited by G.M. Stocks and A. Gonis (Kluwer, Dordrecht, 1989), p. 293.
- <sup>25</sup>R. Tetot, A. Finel, and F. Ducastelle, *J. Stat. Phys.* **61**, 121 (1990).
- <sup>26</sup>A. Finel, V. Mazauric, and F. Ducastelle, *J. Phys. (Paris)* **51**, 1 (1990).
- <sup>27</sup>A. Finel, in *Statics and Dynamics of Alloy Phase Transformations*, Vol. 319 of NATO Advanced Study Institute, Series B, edited by A. Gonis and P. E. A. Turchi (Plenum, New York, 1994).
- <sup>28</sup>D. de Fontaine, *Cluster Approach to Order-Disorder Transformations in Alloys*, Vol. 47 of *Solid State Physics* (Academic, New York, 1994), pp. 33–176.
- <sup>29</sup>J. Sanchez and D. de Fontaine, *Phys. Rev. B* **21**, 216 (1980).
- <sup>30</sup>J. Sanchez and D. de Fontaine, *Phys. Rev. B* **25**, 1759 (1985).
- <sup>31</sup>A. Finel and F. Ducastelle, *Europhys. Lett.* **1**, 135 (1986).
- <sup>32</sup>Y. G. Sinai, *Theory of Phase Transitions: Rigorous Results* (Pergamon, New York, 1982).
- <sup>33</sup>J. Slawny, in *Phase Transitions and Critical Phenomena*, edited by C. Domb and J. L. Lebowitz (Academic, London, 1987), Vol. 11, Chap. 3, pp. 127–205.
- <sup>34</sup>R.W. Hyland, M. Asta, S.M. Foiles, and C.L. Rohrer, *Acta Mater.* **46**, 3667 (1998).
- <sup>35</sup>M. Asta, S.M. Foiles, and A.A. Quong, *Phys. Rev. B* **57**, 11 265 (1998).
- <sup>36</sup>V. Mazauric and S. Nasu, *Mater. Trans., JIM* **35**, 491 (1994).
- <sup>37</sup>D.W. Pashley and A.E.B. Presland, *J. Inst. Met.* **419**, 1958 (1987).
- <sup>38</sup>B. Zhang, M. Lelovic, and W. Soffa, *Scr. Mater.* **25**, 1577 (1991).
- <sup>39</sup>X.D. Zhang and M.H. Loretto, *Philos. Mag. Lett.* **68**, 289 (1993).
- <sup>40</sup>X. Zhang, Y. Li, M.J. Kaufman, and M. Loretto, *Acta Mater.* **44**, 3735 (1996).
- <sup>41</sup>G. Inden and W. Pitsch, *Phase Transformations in Materials*, Vol. 5 of *Materials Science and Technology* (VCH, Weinheim, 1991), Chap. 9, pp. 497–552.
- <sup>42</sup>V. Mazauric, Ph.D. thesis, Université Paris XI, Orsay, France, 1992.
- <sup>43</sup>V. Mazauric, *J. Magn. Magn. Mater.* **126**, 615 (1993).
- <sup>44</sup>This does not mean that the roughening transition is out of the scope of the cluster variation method or, more generally, of a mean-field theory. In fact, an analysis of the generalized susceptibility matrix may be used to localize a roughening transition. This approach consists in looking for the singularities of the matrix of the second derivative of the free energy functional (which is the inverse of the susceptibility matrix) for a 3D system that contains an interface with a step. For more details, see Refs. 42 and 43.